Influence of external flows on crystal growth: Numerical investigation

Dmitry Medvedev,[1,2] Thomas Fischaleck,[1] and Klaus Kassner[1,*]
[1]*Institut für Theoretische Physik, Otto-von-Guericke-Universität Magdeburg, Postfach 4120, D-39016 Magdeburg, Germany*
[2]*Institute of Hydrodynamics of the Russian Academy of Sciences, Novosibirsk, Russia*
(Received 27 April 2006; revised manuscript received 28 July 2006; published 19 September 2006)

We use a combined phase-field–lattice-Boltzmann scheme [Medvedev and Kassner, Phys. Rev. E **72**, 056703 (2005)] to simulate nonfaceted crystal growth from an undercooled melt in external flows. Selected growth parameters are determined numerically. For growth patterns at moderate to high undercooling and relatively large anisotropy, the values of the tip radius and selection parameter plotted as a function of the Péclet number fall approximately on single curves. Hence, it may be argued that a parallel flow changes the selected tip radius and growth velocity solely by modifying (increasing) the Péclet number. This has interesting implications for the availability of current selection theories as predictors of growth characteristics under flow. At smaller anisotropy, a modification of the morphology diagram in the plane of undercooling versus anisotropy is observed. The transition line from dendrites to doublons is shifted in favor of dendritic patterns, which become faster than doublons as the flow speed is increased, thus rendering the basin of attraction of dendritic structures larger. For small anisotropy and Prandtl number, we find oscillations of the tip velocity in the presence of flow. On increasing the fluid viscosity or decreasing the flow velocity, we observe a reduction in the amplitude of these oscillations.

DOI: 10.1103/PhysRevE.74.031606 PACS number(s): 68.70.+w, 02.70.−c, 47.54.−r, 47.20.Hw

I. INTRODUCTION

Crystal growth from the melt or from solution almost never occurs in convection-free conditions. Notwithstanding this fact, models of solidification often focus, when dealing with aspects of morphological stability and pattern formation, on situations where convection is absent [1–4]. Rather than by the negligibility of convective effects, such a choice is generally motivated by the difficulty of including them and the argument that the basic prototypes of patterns appear and may be studied without convection. This in turn has led to the tailoring of experiments on dendritic growth, in which it was explicitly tried to avoid disturbing flows [4–7].

When convection was taken into account in calculations, it was usually in simplified geometries or in conditions enabling simplification of the model [8–10]; often the moving-boundary aspect of the problem was neglected [11,12]. Attempts to model the full problem including convection and the motion of the liquid-solid interface were essentially made only in cases where the deflection of the interface remained relatively small [13,14]. The state of the art a decade ago may be summarized roughly by saying that pattern formation in crystal growth could be well simulated either for the solid, treating the free-boundary problem in its full complexity, or for the liquid, obtaining the convection roll pattern with good accuracy by use of simplifying assumptions for interface motion.

With the advent of efficient phase-field techniques [15], the solution of the moving-boundary problem became simpler, and first simulations of convection in dendritic growth were performed in diverse geometries and with both imposed flows and natural convection [16–18]. In these, the Navier-Stokes equations were solved by standard numerical approaches implementing the partial differential equations either within a finite-element or a finite-difference scheme. It was then a natural idea to supplement the efficient approach to interface motion by an efficient noniterative method for flow simulation, the lattice-Boltzmann scheme. This approach was pioneered by Miller *et al.* [19–21], and a slightly different variant, the advantages of which will be discussed in Sec. II, was developed by ourselves [22,23].

Numerical studies of pattern formation solving the combined free-boundary and flow problems will be useful in guiding the development of analytic selection theory for dendritic growth and other growth modes in the presence of convection. At present, there is a well-developed theory for purely diffusion-limited dendritic growth, in both two and three dimensions [24–31]. It provides an analytic demonstration of the existence of a discrete set of needle crystal solutions to the model equations and shows that the fastest of these solutions is linearly stable.

Acceptance of this microscopic solvability theory has not been uncontroversial, as there is no clear agreement of its predictions referring to crystalline anisotropy with experimental results [32]. On the other hand, the mathematical statements of the theory can hardly be disputed. Therefore, the existence of a needle crystal solution is a fact and its stability shows that it is an attractor of the dynamics. In principle, its basin of attraction might be so small as to render it irrelevant experimentally. But this is essentially excluded by numerical simulations that have shown in both two [33,34] and three [35] dimensions that the dynamical state of the system more or less automatically approaches the prediction of selection theory. In two dimensions at least, this is also true for the dendrite decorated with side branches. Numerics and theory agree with each other so that experimental discrepancies are most likely due to the fact that anisotropies in real crystals do not correspond to the model expressions used in the theory or else that additional effects interfere

*Corresponding author. FAX: +49-0391-6711205. Email address: Klaus.Kassner@physik.uni-magdeburg.de

which are absent or controlled in the simulations (for example, thermal fluctuations not considered in the deterministic theory might affect the operating point of the dendrite at low undercoolings [36]).

One of the more surprising predictions of microscopic solvability theory was the nonexistence of dendrites in the absence of any kind of anisotropy, be it that of surface tension or of interface kinetics. Due to the nature of the theoretical approach, which is singular perturbation theory about an Ivantsov parabola or paraboloid [37], such a statement can hold only for needle crystals with a shape close to the (exact) solution of which they are supposed to be small perturbations. And it turned out later that indeed steady-state crystal growth at zero anisotropy is possible, but only with a shape that is far from an Ivantsov solution. These new structures were called doublons [34] in two dimensions and selection theory has been developed for them as well [38]. Since they continue to exist at finite anisotropy, there is a coexistence range with dendrites, which means that there are two attractors of the dynamics. The standard argument is then that the faster of the two morphologies will win, which in the analytically tractable case is the doublon, whenever it exists.

Large-scale two-dimensional structures consist of arrays of dendrites or of doublons evolving in a noisy environment via side branching and/or tip splitting processes. A theoretical description of the resulting dendrite and seaweed morphologies, based on scaling arguments and selection theory [39] gives a kinetic phase diagram in the parameter space of undercooling versus surface tension anisotropy. All of the analytic predictions mentioned so far refer to diffusion-limited growth only.

A first attempt to extend selection theory to situations with a flow was made by Bouissou and Pelcé [40] and there were a number of less rigorous approaches to the problem as well (references are given in [23]). However, while one experiment seems to support this theory [41], another one contradicts it [42]. Moreover, the theory is based on a linearization of the basic equations, an approach that has been found not to always be reliable [43]. Clearly, more numerical or experimental data are needed to both check the existing theories and guide further theoretical development. The purpose of this paper is to provide first elements of these data using our combined phase-field–lattice-Boltzmann approach [22,23]. A successful selection theory on the microscale (constructed on the basis of these and similar data) would then yield useful information for more applied work on macrosegregation and related questions.

The paper is organized as follows. In Sec. II, we discuss the basic model equations and describe the method of their numerical implementation. In Sec. III, we consider the influence of a parallel flow on the selection of growth velocity and tip radius, whereas in Sec. IV, changes in the position of the morphology transition from dendrites to doublons induced by the flow are discussed. Some concluding remarks are given in Sec. V.

II. MODEL EQUATIONS AND IMPLEMENTATION

For simplicity, we consider a symmetric model with equal thermal diffusivities of the solid and liquid phases, expecting it to display all the qualitative features of the more general case. Moreover, since we wish to confront our simulations with theoretical results on different morphologies, we restrict ourselves to two-dimensional systems here. So far, there are very few results on nondendritic structures in three dimensions.

The well-accepted sharp-interface description of nonfaceted crystal growth from a supercooled melt in the presence of a fluid flow with velocity $\mathbf{U}$ then starts from the following set of bulk and interface equations:

$$\partial_t u + \mathbf{U}\nabla u = D\nabla^2 u,$$

$$\mathbf{n}\cdot\mathbf{V} = D\mathbf{n}\cdot(\nabla u|_s - \nabla u|_l),$$

$$u_i = -d(\theta)/R_K - \beta\mathbf{n}\cdot\mathbf{V}. \tag{1}$$

Herein, $u=c_p(T-T_m)/L$ with c_p denoting the heat capacity and L the latent heat, both per unit volume, is a nondimensionalized temperature, T being the temperature at the considered position and T_m the bulk melting temperature. D is the thermal diffusivity, $\mathbf{n}$ the local normal to the liquid-solid interface (pointing from the solid into the liquid), and $\mathbf{V}$ the interface velocity. The subscripts of the temperature gradients in the second equation refer to the solid and the liquid sides of the interface, respectively. $d(\theta)$ is the capillary length, related to the orientation-dependent surface tension $\gamma(\theta)$ by $d(\theta)=(d_0/\gamma_0)[\gamma(\theta)+\gamma''(\theta)]$. θ is the angle between the interface normal and some fixed direction (usually identified with the x axis of the coordinate system), γ_0 the average of the interface tension over all orientations, and $d_0=\gamma_0 T_m c_p/L^2$ the similarly averaged capillary length. R_K is the local radius of curvature and β the kinetic coefficient. In principle, β is an orientation-dependent quantity just as the surface tension; however, we will restrict ourselves to the case of fast attachment kinetics here, meaning that β becomes negligible. This implies certain constraints on the choice of parameters of the phase-field model (see below).

The boundary condition for the normal velocity is usually referred to as the Stefan condition, while the last equation in (1), describing the interface temperature, is the Gibbs-Thomson relation (for $\beta=0$) with kinetic correction (for $\beta\neq 0$).

At infinity, the temperature in the solid approaches T_m, corresponding to $u=0$, whereas in the liquid, it takes on some value $T_\infty<T_m$, corresponding to $u=-\Delta$. The quantity Δ is denoted as the nondimensional undercooling.

In order not to complicate things unnecessarily, we assume the melt to be an incompressible Newtonian fluid, governed by the appropriate version of the Navier-Stokes equations, supplemented by boundary conditions at the interface

$$\partial_t\mathbf{U} + \mathbf{U}\nabla\mathbf{U} = -\frac{\nabla P}{\rho} + \nu\nabla^2\mathbf{U},$$

$$\nabla\cdot\mathbf{U} = 0,$$

$$\mathbf{U}_i = 0, \tag{2}$$

where equal mass densities ρ have been assumed in the two phases, ν is the kinematic viscosity, and P denotes the pressure of the liquid. $\mathbf{U}_i$ is the flow velocity at the interface. The boundary conditions correspond to no-slip conditions for the tangential velocity and describe the fact that, for equal densities of the two phases, the liquid is neither sucked toward nor rejected from the interface; hence, its normal velocity at the interface is zero in the laboratory frame (the rest frame of the solid).

It is convenient to use dimensionless variables in the analysis of the growth process. The tip radius can be nondimensionalized using the capillary length as $\bar{R}=R/d_0$, whereas flow and growth velocities become nondimensional via normalization with the characteristic velocity given by the ratio of the thermal diffusion coefficient and the average capillary length, that is, $\bar{U}=Ud_0/D$ and $\bar{V}=Vd_0/D$.

The material properties are characterized by the anisotropy of the surface energy or rather that of the capillary length and by the Prandtl number $\mathrm{Pr}=\nu/D$; the flow is characterized by the Reynolds number $\mathrm{Re}=UR/\nu$.

We employ a combined phase-field–lattice-Boltzmann scheme where solidification is simulated with the phase-field model of Karma and Rappel [35,44], and the flow of the liquid as well as convective and diffusive heat transport are modeled using a lattice-Boltzmann (LB) method. This means that the actual equations simulated are not those given above but a phase-field approximation to the interface dynamics (involving a finite-width transition region between the solid and its melt) and a set of kinetic equations that are asymptotically equivalent to the Navier-Stokes and advection-diffusion equations.

In particular, the phase-field equations read

$$\tau(\theta)\partial_t\psi = [\psi - \lambda u(1-\psi^2)](1-\psi^2) + \boldsymbol{\nabla}\cdot[W^2(\theta)\boldsymbol{\nabla}\psi] - \partial_x[W(\theta)W'(\theta)\partial_y\psi] + \partial_y[W(\theta)W'(\theta)\partial_x\psi],$$

$$\partial_t u + \mathbf{U}\boldsymbol{\nabla}u = D\nabla^2 u + \frac{1}{2}\partial_t h(\psi). \tag{3}$$

The value $\psi=1$ of the phase-field variable is chosen to represent the solid phase, whereas $\psi=-1$ corresponds to the liquid phase. $W(\theta)$ is an anisotropic interface width, $\tau(\theta)$ a relaxation time, and $\theta=\arctan(\partial_y\psi/\partial_x\psi)$ the angle between the normal on a level set of ψ and the x axis. For the level set given by $\psi=0$, this angle is the same as the angle θ in Eq. (1); otherwise it provides an extension of the definition of the latter into the bulk. $h(\psi)$ describes the coupling of the diffusion field to the phase field via latent heat production. This function was chosen as $h(\psi)=\psi$, which appears to be computationally most efficient [35].

Via a suitable asymptotic expansion, the equations of the sharp-interface model (1) can be derived [35], with the following expressions for the capillary length and kinetic coefficient:

$$d(\theta) = \frac{I}{\lambda J}[W(\theta) + \partial_\theta^2 W(\theta)],$$

$$\beta(\theta) = \frac{I}{\lambda J}\frac{\tau(\theta)}{W(\theta)}\left(1 - \lambda\frac{K+JF}{2I}\frac{W^2(\theta)}{\tau(\theta)}\right).$$

These equations, first given by Karma and Rappel [44], have been shown to be equivalent to a second-order accurate standard asymptotic approximation [35,45].

Requiring

$$W = W_0 A(\theta), \quad \tau = \tau_0 A^2(\theta), \quad \lambda = \frac{2ID\tau_0}{(K+JF)W_0^2},$$

we can impose a vanishing kinetic coefficient [44]. For $h(\psi)=\psi$, the values of the phase-field specific coefficients are $I=2\sqrt{2}/3$, $J=16/15$, $K=\sqrt{2}(\frac{188}{225}-\frac{16}{15}\ln 2)$, and $F=\sqrt{2}\ln 2$ [23,35,44]. We use the anisotropy function

$$A(\theta) \equiv \frac{\gamma(\theta)}{\gamma_0} = 1 + \frac{\alpha}{15}\cos 4\theta,$$

leading to

$$d = d_0(1 - \alpha\cos 4\theta), \tag{4}$$

which is the usual model expression exhibiting fourfold symmetry.

Moreover, we set $\tau_0=1, W_0=1$.

The equation for the phase field ψ was discretized on a uniform spatial lattice with grid spacing $\Delta x=0.4$, and it was solved using the explicit Euler method with constant time step Δt in the range 0.008–0.016.

Both the flow of the liquid and the heat transport are simulated using the LBGK method (see [46]). Its main variables are one-particle distribution functions f_k defined on the nodes of a regular spatial lattice. Different labels k correspond to different velocities $\mathbf{c}_k$ from a fixed finite set. In the two-dimensional model used here, we employ nine velocities, namely, $\mathbf{c}_0=(0,0)$, $\mathbf{c}_k=(\cos[(k-1)\pi/2],\sin[(k-1)\pi/2])\delta x/\delta t$ for $k=1,\ldots,4$, and $\mathbf{c}_k=\sqrt{2}((\cos[(k-1/2)\pi/2],\sin[(k-1/2)\pi/2])\delta x/\delta t$ for $k=5,\ldots,8$. Here, δx is the grid spacing, equal for both directions, and δt is the time step. The effect of making the velocities proportional to $\delta x/\delta t$ is that nonzero velocities lead to nearest-neighbor and next-nearest-neighbor sites of the square lattice in one time step, i.e., only lattice point positions appear in the dynamics; no interpolations are necessary.

Inside the LB equation part of our simulations, the grid spacing and time step are both formally rescaled to 1, which is the reason why we have used a different notation for them here from that in the phase-field part of the simulation (δx and δt vs Δx and Δt), although they are actually the same "material" quantities.

The evolution equation for f_k is

$$f_k(t+\delta t, \mathbf{x}+\mathbf{c}_k\delta t) = f_k(t,\mathbf{x}) + \frac{f_k^{eq} - f_k}{\tau_f}\delta t. \tag{5}$$

Distribution functions are advected [first term on the right-hand side (RHS)] and undergo a relaxation to equilibrium values f_k^{eq} which are, as usual, taken to be expansions of

Maxwellians up to second order in the fluid velocity $\mathbf{U}$,

$$f_k^{eq} = \rho w_k \left(1 + \frac{\mathbf{c}_k \cdot \mathbf{U}}{c_s^2} + \frac{(\mathbf{c}_k \cdot \mathbf{U})^2}{2c_s^4} - \frac{U^2}{2c_s^2} \right), \tag{6}$$

with c_s having the physical meaning of an isothermal sound velocity. The local fluid density is given by $\rho = \Sigma_k f_k = \Sigma_k f_k^{eq}$, the flow velocity is $\mathbf{U} = \Sigma_k f_k \mathbf{c}_k / \rho$, and the weight coefficients are $w_0 = 4/9$, $w_{1-4} = 1/9$, $w_{5-8} = 1/36$. This form of the equilibrium distribution functions ensures mass and momentum conservation and provides the correct form of the momentum flux tensor [46,47].

Performing a Chapman-Enskog expansion, one can derive from (5) the continuity and Navier-Stokes equations [46], with kinematic viscosity $\nu = c_s^2(\tau_f - \delta t/2)$. The isothermal sound velocity is $c_s = \delta x / \sqrt{3}\delta t$; for small flow velocities the fluid is almost incompressible (effects of compressibility are proportional to U^2/c_s^2).

The influence of the growing pattern on the fluid flow was simulated as proposed in [17,18]. An additional dissipative force was introduced in partially filled regions

$$\mathbf{F}_d = -\rho\nu \frac{2g\phi^2}{W_0^2}\mathbf{U},$$

where $g = 2.757$ and $\phi = (1+\psi)/2$ is the solid fraction. This provides the correct velocity boundary conditions at the diffuse interface (see [17,18]), i.e., the sharp-interface limit of the velocity boundary conditions of Eq. (2) is correctly reproduced. The value of the constant g was obtained in [17,18] by an asymptotic analysis of plane flow past the diffusive interface.

The action of forces on a liquid was simulated by the exact difference method of [48]. The term $\Delta f_k = f_k^{eq}(\rho, \mathbf{U} + \Delta\mathbf{U}) - f_k^{eq}(\rho, \mathbf{U})$ is added to the RHS of Eq. (5), where $\Delta\mathbf{U} = \mathbf{F}\delta t/\rho$ is the velocity change due to the action of force $\mathbf{F}$ during time step δt. This form of the change of the distribution functions is exact in the case where the distribution is equilibrium before the action of the force (then after the action the distribution remains equilibrium), hence the name of the method. In the case of a nonequilibrium initial state, this method is accurate to second order in $\Delta\mathbf{U}$. It is simple enough and valid for arbitrary lattices and any dimension of space.

The heat transport equation in (3) was treated in a very similar way via the introduction of nine additional distribution functions $N_k(t, \mathbf{x})$. An extensive discussion of these algorithmic details is presented in [23].

In order to give a general impression of the type of results obtainable with these simulations, we display Figs. 1 and 2, showing the steady states of a dendritic and a doublon pattern, respectively.

A few remarks may be in order comparing our model with its main predecessor as given by Miller *et al.* [19–21]. There are obvious similarities, but our approach is simpler in the lattice-Boltzmann part and has better convergence in the phase-field part. The model discussed in [19–21] is four dimensional and uses 24 velocities. We have a two-dimensional model with 2×9 velocities and our collision matrix is simpler. So the lattice-Boltzmann part of our model is faster in two dimensions, which is the only case considered here.

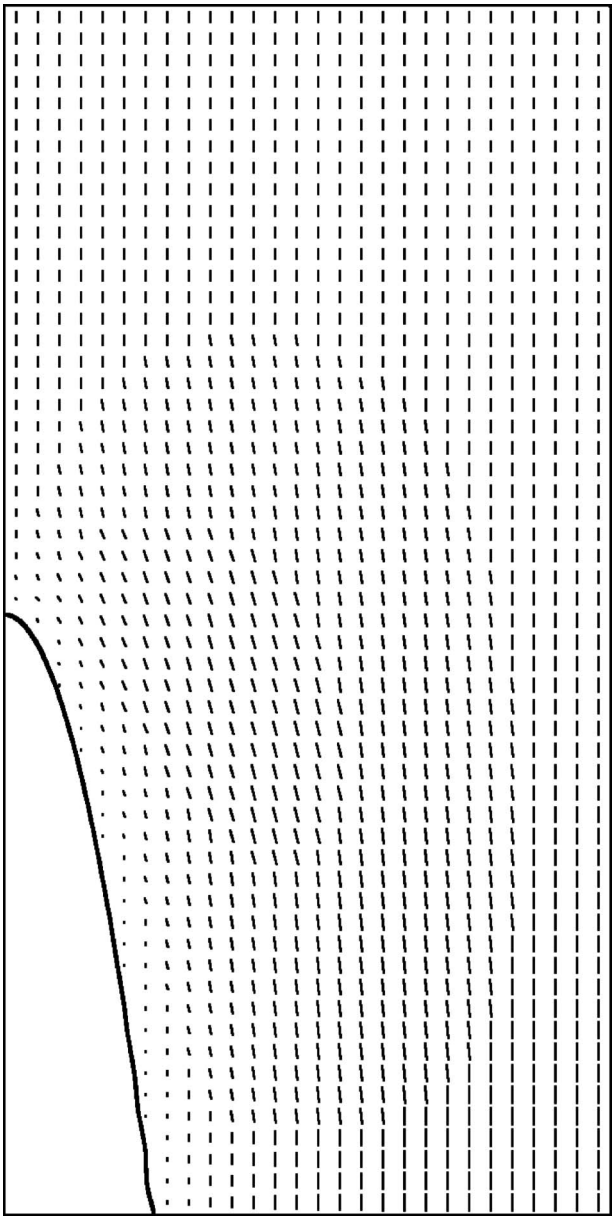

FIG. 1. Symmetric needle crystal, i.e., dendritic pattern in antiparallel flow. Growth parameters: $\Delta = 0.75$, $\alpha = 0.45$, $\bar{U} = 0.01$. The capillary length is $d_0 = 0.185$, the measured growth velocity $\bar{V} = 0.0451$, leading to a diffusion length of 8.2 (20.5 lattice units). The flow pattern is indicated by the streaks outside the crystal. Numerical grid size: 700×1400 corresponding to $1513.5d_0 \times 3027.0d_0$.

Concerning the phase-field part, our approach includes the Karma model which has been shown to be quantitative at much larger interface thicknesses than previous alternatives. The phase-field model used by Miller *et al.* has not been demonstrated to have any of the advantages of the thin-interface asymptotics. Its quantitative accuracy might be challenged on the basis of the same objections as the original Kobayashi model [49].

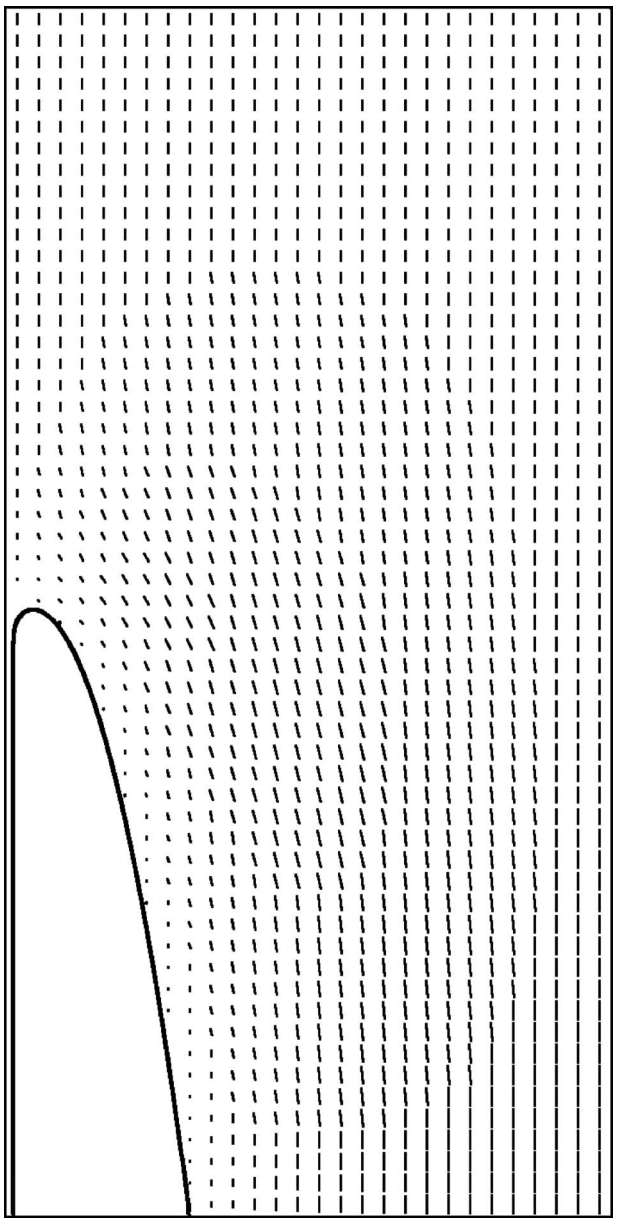

FIG. 2. Asymmetric needle crystal, (half of a) doublon pattern. Same growth parameters as in Fig. 1, except that $\alpha=0.3$. The capillary length and system size are the same as in Fig. 1 as well, the measured growth velocity is $\bar{V}=0.0402$, leading to a diffusion length of 9.2 or 23 lattice units.

Therefore, with the same accuracy prescribed, we expect the phase-field part of our model to be much more efficient (because it converges to the correct sharp-interface limit at much smaller system sizes) than that of the model used in [19–21] and the lattice-Boltzmann part to be slightly more efficient.

III. SELECTION OF GROWTH PARAMETERS

The growth of a single needle crystal in parallel flow was simulated for fixed surface tension anisotropy and a range of undercoolings and flow velocities. To investigate the effects of parallel flow on the growth characteristics, needle crystals grown without flow were used as initial configurations. Reaching the steady state in the absence of flow took between 90 000 and 300 000 time steps.

After loading the values of the temperature and phase fields, the flow was initialized with boundary conditions of constant flow velocity perpendicular to the upper boundary and zero velocity gradients at the lower boundary, while the side boundaries were made reflecting. First, the flow was allowed to evolve with a fixed configuration of the solid, and the relative velocity error was calculated at each time step as

$$U_{err}=\frac{\sum|\hat{U}_x-U_x|+|\hat{U}_y-U_y|}{\sum|U_x|+|U_y|}.$$

Here, $\hat{\mathbf{U}}$ refers to the flow velocity at the current and $\mathbf{U}$ to that at the preceding time step; the summation is over all grid nodes. The convergence condition was $U_{err}\leq 10^{-5}$.

Then the growth of the pattern was "switched on" and continued until a steady, i.e., constant-velocity, state was reached. In the range of undercoolings $0.72<\Delta<0.76$, this took on the order of 150 000 time steps.

The numerical grid in these runs had a size of 700×1400, corresponding to between $505d_0\times 1010d_0$ and $2014d_0\times 4028d_0$. For the smallest measured velocities, the diffusion length remained below 250 lattice units; for the largest one, it was about 15 lattice units. Therefore, in all cases the system size was large enough to consider finite-size effects negligible, in particular in view of the fact that the computational domain corresponded to half the system size only (see Figs. 1 and 2).

All the simulations discussed in this section were done either until convergence of the pattern to a steady state was achieved or such a steady state was found to be unattainable—below we report on the appearance of oscillatory states in certain parameter regions. Only then were growth characteristics such as the growth velocity measured, i.e., care was taken to avoid transient states providing only information about temporary growth characteristics.

Computed values of the reduced tip radius $\bar{R}$ and selection parameter $\sigma=2Dd_0/R^2V=2/\bar{R}^2\bar{V}$ are plotted versus the growth Péclet number $\mathrm{Pe}=RV/2D=\bar{R}\bar{V}/2$ in Figs. 3(a) and 3(b) for dendrites (single symmetric fingers). In the figure, the anisotropy of surface stiffness is $\alpha=0.75$, the range of nondimensional initial undercoolings $\Delta=c_p(T_m-T_\infty)/L$ extends from 0.4 to 0.8, and the reduced flow velocity $\bar{U}=Ud_0/D$ is typically chosen between 0 and 0.32 (0, 0.01, 0.02, 0.04, etc.). One can see that for each of the two data sets most of the points fall onto a unique curve. Minor deviations appear mainly for small Prandtl numbers and large flow velocities. The range of Reynolds numbers investigated in this data set was $0\leq\mathrm{Re}\leq 5.6$. It is possible to define a relative Reynolds number based on the flow speed in the reference system attached to the surface of the growing crystal. This Reynolds number, which was never zero, of course, extended up to ≈ 7.1.

To obtain the tip radius, we fitted a parabola to an extended region about the tip. This procedure does not yield an

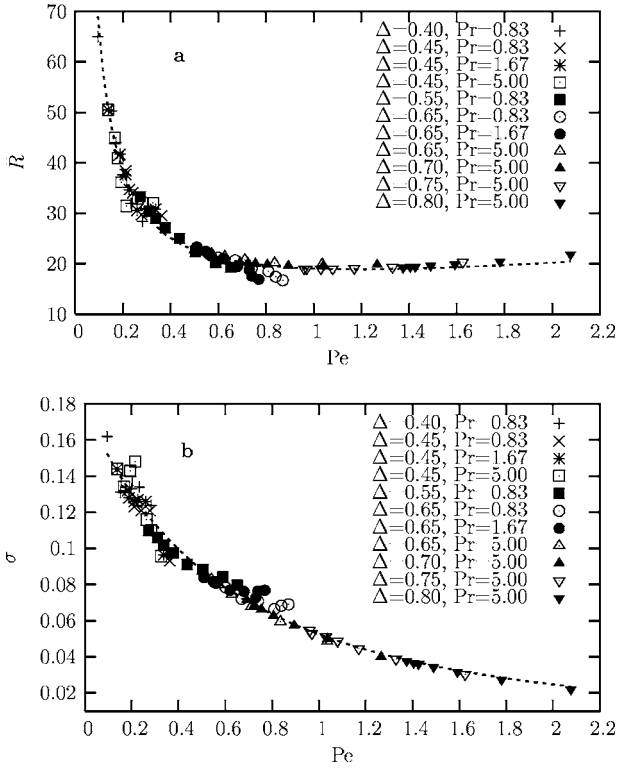

FIG. 3. Dependence of the tip radius (a) and selection parameter σ (b) on the Péclet number for dendrites. Anisotropy parameter $\alpha=0.75$. Each symbol corresponds to the undercoolings and Prandtl numbers given in the legend and a value of the velocity $\bar{U}$ of the imposed flow in the range from 0 to 0.32. Larger values of $\bar{U}$ correspond to larger Péclet numbers. The dashed line in (b) is a fit to $f(\mathrm{Pe})=a/(1+b\,\mathrm{Pe})^2$, the dashed line in (a) is computed as $g(\mathrm{Pe})=1/[f(\mathrm{Pe})\mathrm{Pe}]$. From the fit, $a=0.178$, $b=0.841$.

approximation to the inverse curvature at the tip itself, because due to anisotropy, the shape deviates from a parabola close to the tip [50]. Rather, it defines the tip radius by a global parabolic envelope associated with energy conservation; the Péclet number Pe calculated from this tip radius corresponds to the Péclet number used in selection theory and in the absence of flow reduces to the Ivantsov value, defined by $\Delta=\sqrt{\pi\mathrm{Pe}}\exp(\mathrm{Pe})\mathrm{erfc}(\sqrt{\mathrm{Pe}})$.

The tip radius initially decreases with increasing Péclet number but later begins to increase again (for this anisotropy, the minimum is at about Pe=1), while the selection parameter σ decreases in the whole range of Péclet numbers investigated. That the tip radius increases for large undercooling can be easily understood: in the limit $\Delta=1$, the solution should approach a planar front with $\bar{R}=\infty$. This argument is made more quantitative below.

From the theoretical point of view, the most interesting feature of these results is the existence of a master curve, on which the data fall for a wide range of parameters. For this feature (if it holds generally) allows us to use the theory of dendritic growth without convection to make predictions of selected velocities and tip radii in the presence of a forced flow. In the absence of flow, the growth Péclet number depends only on the undercooling. As soon as flow is introduced, the Péclet number depends both on the undercooling and the velocity of the imposed flow. What Fig. 3(b) then tells us is essentially that no matter how we produce a given Péclet number, we should expect the same selected value of σ at fixed anisotropy. Hence, if we change both the flow velocity and the undercooling in a way that keeps the Péclet number constant, the growth speed and shape remain unchanged. This means that the case with flow can be mapped to the case without flow. Of course, the problem of determining the Péclet number, for given undercooling and flow velocity at infinity, is in itself a nontrivial task. In limiting cases (small external flow speed), it may be approximated by the value obtained for an Ivantsov-type solution of an Oseen approximation to the problem with flow.

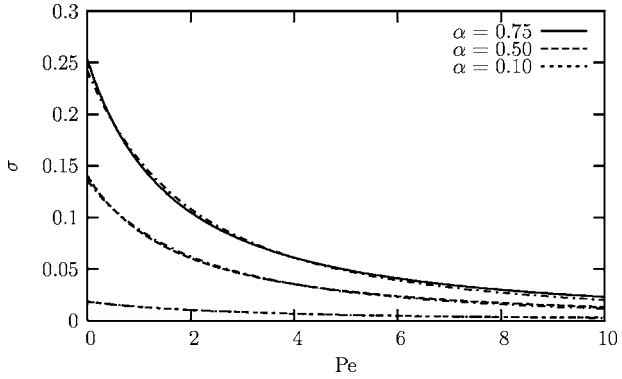

FIG. 4. Behavior of the selection parameter as a function of the Péclet number according to the linearized version of selection theory as given in [52]. The dash-dotted lines are fits with the same analytic expression as in Fig. 3(b).

According to selection theory for the purely diffusion-limited case, we should expect σ to become independent of the Péclet number for small anisotropy and small undercooling. The latter condition can be relaxed [51]—as long as $\mathrm{Pe}\,\alpha^{1/2}\ll 1$, the standard result of selection theory, $V\sim(D/d_0)\alpha^{7/4}\mathrm{Pe}^2$, continues to hold for a model anisotropy of the type (4). However, due to computational limitations, this limit is difficult to access, hence neither of these conditions is well satisfied in Fig. 3(b), where $\alpha=0.75$ and Pe varies through 1. The opposite limit of large Péclet number is also known analytically [51]; the selection parameter should vary, for fixed small anisotropy, proportional to $1/\mathrm{Pe}^2$. Moreover, it is possible to evaluate the predictions of solvability theory [52] numerically for arbitrary Péclet numbers. Formally, this can be done for arbitrary values of the anisotropy parameter α—three examples are exhibited in Fig. 4—but the theory should not be expected to yield good results for anisotropies that are not sufficiently small.

Comparing Fig. 3 with Fig. 4, we see that the numerical results and the predictions from solvability theory show the same general trend of σ decreasing with increasing Péclet number and that the order of magnitude of our σ values is the same as for $\alpha=0.75$ in solvability theory. However, the selection parameter decreases much faster with increasing Péclet number than in the theory (note the different scales of the Pe axes). This may not be too surprising—after all the theory is made only for $\alpha\ll 1$, and while it has been claimed to be quantitatively not too bad for α up to 0.5 or 0.6 [52],

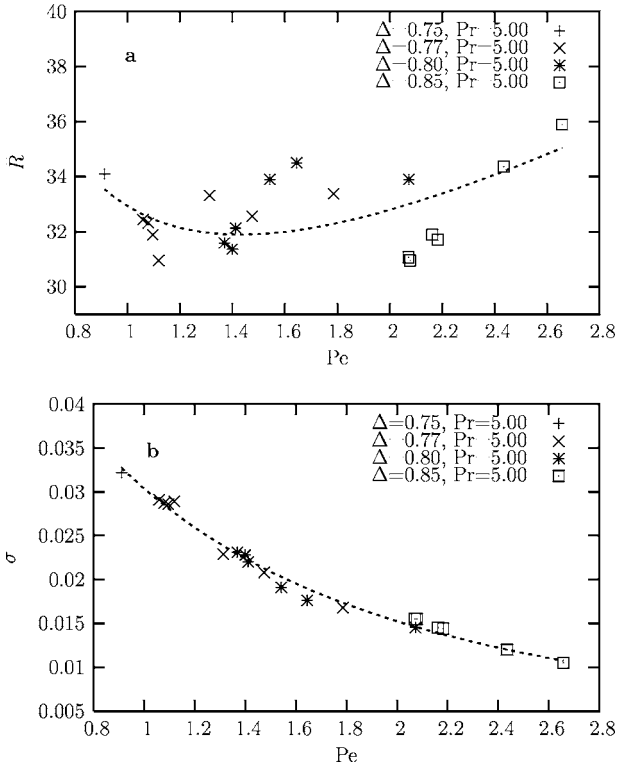

FIG. 5. Dependence of the tip radius (a) and selection parameter σ (b) on the Péclet number for doublons. Anisotropy parameter $\alpha=0.3$. Appearance of the same symbol several times means different values for $\bar{U}$ (in the same range as in Fig. 1) at the same pair of values for the undercooling and the Prandtl number. The dashed lines are obtained by fitting as in Fig. 3, which yields $a=0.0876$, $b=0.699$.

this claim referred to the small Péclet number case. Since the Péclet number appears only at next-to-leading order in the small parameter of the theory ($\sqrt{\sigma}$), it is perhaps not unreasonable to assume that the dependence of selected characteristics on it is described less accurately within the theory than, say, the anisotropy dependence at Pe=0.

Because the theory predicts the limiting behaviors of the selection parameter at small and large Péclet numbers, it is tempting to try to capture the behavior at intermediate Pe by a simple interpolating function. The simplest rational function approaching a constant value for $\mathrm{Pe}\to 0$ at finite slope and being proportional to $1/\mathrm{Pe}^2$ at large Pe is $f(\mathrm{Pe})=a/(1+b\mathrm{Pe})^2$. Fits with this function work pretty well for both our numerical data and the results from selection theory as is demonstrated in Figs. 3 and 4. Because $\bar{R}=1/(\sigma\mathrm{Pe})$, this also yields a description of the tip radii in Fig. 3(a) as well as a quantitative estimate for the tip radius behavior at large Pe ($\sim \mathrm{Pe}\, b^2/a$). The value of a gives the limit of the selection parameter for Pe=0, which in our case is about 30% below the value obtained from selection theory (for an illegitimately large value of α).

Note that given the graphs of $\sigma(\mathrm{Pe})$ and $\bar{R}(\mathrm{Pe})$, we could obtain a similar representation for the growth velocity simply by plotting $\bar{V}=2/(\sigma\bar{R}^2)$ or, even simpler, $\bar{V}=2\sigma\,\mathrm{Pe}^2$. Hence, the limiting growth velocity for $\mathrm{Pe}\to\infty$ is $\bar{V}=2a/b^2$.

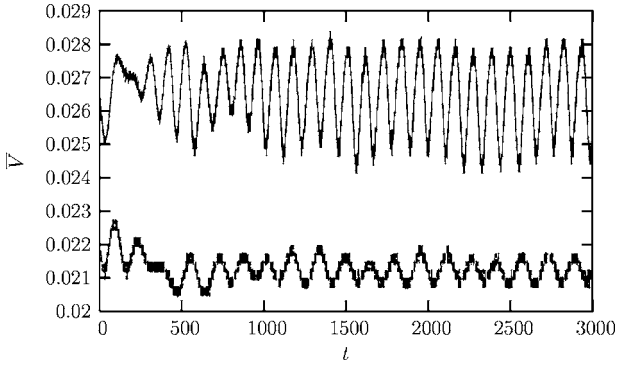

FIG. 6. Measured growth velocity $\bar{V}$ of a dendrite as a function of time t. $\Delta=0.7$, $\alpha=0.15$, $\bar{U}=0.04$; the upper curve corresponds to Pr=1.78, the lower one to Pr=5.00. The rather strong flow provokes oscillations of the tip speed with large amplitude for small viscosity (Pr=1.78) and small amplitude for large viscosity (Pr=5.00).

Results for doublons, i.e., two asymmetric fingers with a liquid-filled channel between them growing together, are presented in Fig. 5. The surface stiffness anisotropy is 0.30 in this case; the undercooling ranges from 0.77 to 0.85. For the reduced flow velocity the same range from 0 to 0.32 was taken as for the symmetric finger, whereas the Reynolds numbers extended only up to 2.1, as the set of considered viscosities did not contain values as small as those of Fig. 3.

The "tip" radius was measured by fitting a parabola to the exterior shape of the doublon, that is, only points much farther from the central channel than the two tips of the pattern were used in the fitting procedure. Since this procedure depends also on the cutoff value defining which part of the shape is "exterior" and which one is "interior," we do not expect a similar accuracy for this radius as in the case of dendritic patterns. Moreover, the total range of radii displayed is about a factor of 6 smaller than in Fig. 3(a), which contributes to making the results appear much noisier than those for the dendritic pattern.

Nevertheless, while the characteristic length scale of the doublon may not display the same clear-cut universality as that of the dendrite, a unique dependence of the selection parameter on the Péclet number is clearly visible in Fig. 5(b). A fit to the same rational function $f(\mathrm{Pe})$ as in the dendritic case is possible, but less trustworthy than for the dendrites, as the range of accessible Péclet numbers is smaller. Moreover, its theoretical foundation is weaker than for dendrites, as selection theory for doublons does not yet seem to have been worked out in the limit of large Péclet number.

Finally, it should be mentioned that the introduction of an external flow may lead to a loss of stability of steady-state growth and result in instationary patterns. With small anisotropy and Prandtl number, oscillations of the tip velocity are observed. This observation may relate to the prediction by the selection theory presented in [40] that above a certain flow velocity no steady-state solutions will be possible anymore. Increase of the fluid viscosity and/or decrease of flow velocity damps these oscillations as shown in Fig. 6.

From the existence of these oscillations, it may be concluded that there are parameter regions (attained for given anisotropy on decreasing the Prandtl number) where the

simple picture discussed above breaks down. Selected growth characteristics will then not depend on the growth Péclet number and the anisotropy parameter alone. For these oscillations are not predicted by solvability theory without flow, hence the simple mapping to this theory is not feasible anymore, and an extension of selection theory such as the one given in [40], but preferably on a more rigorous basis, becomes necessary.

IV. MORPHOLOGY DIAGRAM

Previously, a kinetic phase diagram was obtained theoretically [39] in the case of purely diffusive growth, distinguishing four morphologies: compact dendritic structures at large anisotropy and not too large undercooling, compact seaweed patterns at large undercooling (and not too large anisotropy), noise-dominated fractal dendritic and seaweed morphologies at sufficiently small anisotropy and undercooling, respectively. The transition lines between the different morphologies and their nature (as first- or second-order kinetic phase transition or crossover) were determined analytically under certain limit assumptions. Regarding the compact growth morphologies, it was stated that doublons cease to exist for larger anisotropies, but when they exist, they are faster than dendrites. In principle, the latter exist at all nonzero anisotropies, but they are overtaken and thus overgrown by doublons in the region of coexistence (hence the transition from compact dendrite to compact seaweed would be first order, because both morphologies coexist above a certain undercooling).

How an imposed external flow may influence the different growth patterns is interesting and largely unexplored. We have already shown that doublons survive in a shear flow [22,23], a somewhat counterintuitive result.

In the present work, we investigate the morphology diagram for growth in a parallel flow imposing a number of different flow velocities, with a particular view to the positions of the transition lines between doublon and dendrite growth.

Figure 7 gives an overview of the measured morphology diagram (actually a small section only of the entire plane undercooling versus anisotropy) for the purely diffusive case and two different flow velocities. In relating this to previously measured transitions between the dendritic and doublon morphologies [34,53] (at zero flow), it should be kept in mind that these older numerical results refer to the *one-sided model* whereas here we consider the *symmetric* model. As it turns out, the transition line is shifted to higher values of the anisotropy (e.g., α between 0.20 and 0.25 at $\Delta=0.7$ instead of $\alpha\approx 0.12$), which seems plausible, because the added diffusion in the solid tends to reduce anisotropy-induced temperature differences imposed at the interface. In fact, phase-field simulations of the symmetric model (in the absence of flow) by Tokunaga and Sakaguchi [54] also exhibit this shift to higher anisotropies. Their calculations were done in a channel that is narrow in comparison with our system width, so they introduced an intermediate morphology between doublons and dendrites, two competing Saffman-Taylor like fingers [55,56] (ST) (the existence range of which should

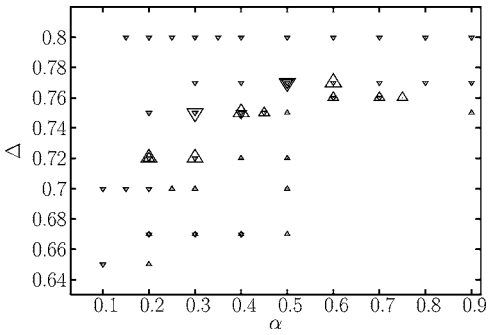

FIG. 7. Morphology diagram displaying the predominance of dendrites or doublons at different flow speeds. Triangles correspond to dendrites being either the only morphology or the faster one, inverted triangles correspond to doublons being faster. There are three sizes of symbols. The smallest triangles refer to the case without flow described in current analytic theories. Medium-size triangles are for a flow speed $\bar{U}=0.01$; big ones for a flow speed $\bar{U}=0.04$. The general trend is that with increasing flow speed dendrites invade the original domain of doublons. There are three points at $\Delta=0.67$, where the simulation gave the same velocities for both structures to three significant digits.

vanish for infinite system size). For $\Delta=0.7$, they find the transition from doublons to ST at $\alpha\approx 0.24$, that from ST to dendrites at $\alpha\approx 0.32$, which agrees well with our result.

Because we simulate only one of the two fingers of a doublon, imposing mirror symmetry about the system boundary (see Fig. 2), our calculation suppresses possible antisymmetric instabilities of a doublon, e.g., instabilities, where one finger gets ahead of the other. However, there is some evidence [34] that on increase of the anisotropy parameter doublons normally get unstable by dynamical unbinding of the two fingers, which move apart and become independent dendrites. This unbinding instability is symmetric and would not be missed by our approach. All our statements about *existence* of doublons are, of course, not affected by the possibility of an unstable mode not taken into account. And finally, we base our assertions about the predominance of one of the two growth modes on comparisons of the velocities of both, which will come out correctly of the computation with the imposed symmetry. The worst that could happen is that a doublon found to be faster than a dendrite at the same parameter values is unstable with respect to an antisymmetric perturbation, in which case the dendritic morphology would survive, if it is stable. Such a scenario is not very likely, given the fact that our doublons, whenever they were faster than the associated dendrites, exhibited closely spaced tips, corresponding to the predictions of selection theory [38].

The case of purely diffusive growth is depicted in Fig. 7 by the smallest symbols. Triangles with their tips pointing upward correspond to dendrites, inverted triangles to doublons. On increase of the reduced flow velocity $\bar{U}$ to 0.01, denoted by larger triangles, dendrites become faster than doublons at several combinations of undercooling and anisotropy. The largest triangles in Fig. 7 correspond to a velocity of $\bar{U}=0.04$. They demonstrate how the region where dendrites are faster than doublons increases with increasing flow velocity.

It should be noted that according to the analytic theory [38] for the purely diffusive case doublons would always be faster than dendrites at coexistence. Dendrites would dominate only where doublons did not exist. This is not quite true at the large anisotropy values considered here. For example, at the point $\alpha=0.5$, $\Delta=0.67$, where we have put a symbol denoting dendritic growth, doublons exist, too, but are slower than dendrites. Nevertheless, it is rather remarkable that external flow can lead to dendrites becoming sufficiently fast to outrun doublons in an extended range of parameters.

Note that the morphology diagram should actually be displayed in three dimensions, as it is spanned by the three variables α, Δ, and $\bar{U}$. We circumvent the need for a genuine three-dimensional (3D) representation by taking different symbol sizes to represent different flows, as only few flow velocity values could be studied.

That the presence of a parallel fluid flow in general favors dendrites over doublons is an additional possible reason for the difficulty to obtain doublons in experiments, the main reason of course being that in experiments the value of the undercooling is usually so small that one is far from the existence region of doublons. Experimental approaches to produce doublons in crystal growth either had to use artifices to obtain effectively vanishing anisotropy in the growth plane [57] or led to the observation of transient doublons only [58,59]—these were, however, true 3D structures.

V. CONCLUSIONS

In summary, we use a previously proposed combined phase-field–lattice-Boltzmann scheme to simulate dendritic growth from a supercooled melt in external counterflows directed parallel to the growing needle crystal. Several regions of the morphology diagram in the space spanned by the anisotropy parameter, the nondimensional undercooling and the nondimensional flow velocity were explored.

For dendrites at moderate to high undercooling and high anisotropy, we found that the values of tip radius and selection parameter, and hence of the growth velocity, depend on the growth Péclet number only, not on the undercooling and flow velocity separately. Hence, it may be argued that the essential effect of a parallel flow, at least in a certain part of parameter space, is to change the selected tip radius and growth velocity solely by modifying (increasing) the Péclet number. In this region, selection theory for the purely diffusive case is applicable, the main task being to determine the relationship between undercooling, imposed flow velocity and the growth Péclet number. For doublons a similar dependence for the selection characteristics was obtained.

Incorporation of genuine flow effects into selection theory does become necessary as the anisotropy and Prandtl number become small, when tip oscillations take over and the steady state either ceases to exist or becomes unstable. Increase of the fluid viscosity and/or decrease of flow velocity is observed to damp down these oscillations.

For smaller anisotropy, an interesting phenomenon is observed. The growth velocity for dendrites increases faster than for doublons with increase of the flow velocity (at the same undercooling and anisotropy). For some parameters, dendrites become faster, and hence external flow can lead to morphology transitions and change the kinetic phase diagram.

ACKNOWLEDGMENTS

Financial support of this work by the German Research Foundation (DFG) under Grant No. FOR 301/2-1 within the framework of the research group "Interface Dynamics in Pattern Forming Processes" is gratefully acknowledged.

[1] H. Müller-Krumbhaar and W. Kurz, in *Phase Transformations in Materials*, edited by R. W. Cahn, P. Haasen, and E. J. Kramer (VCH Verlagsgesellschaft, Weinheim, 1991), p. 553.
[2] B. Billia and R. Trivedi, in *Handbook of Crystal Growth*, edited by D. T. J. Hurle (Elsevier, Amsterdam, 1993), Vol. 1b, p. 899.
[3] S. R. Coriell and G. B. McFadden, in *Handbook of Crystal Growth* (Ref. [2]), Vol. 1b, p. 785.
[4] M. E. Glicksman and S. P. Marsh, in *Handbook of Crystal Growth* (Ref. [2]), Vol. 1b, p. 1075.
[5] M. Glicksman, M. Koss, and E. A. Winsa, Phys. Rev. Lett. **73**, 573 (1994).
[6] J. C. LaCombe, M. B. Koss, V. E. Fradkov, and M. E. Glicksmann, Phys. Rev. E **52**, 2778 (1995).
[7] U. Bisang and J. H. Bilgram, Phys. Rev. E **54**, 5309 (1996).
[8] S. H. Davis, in *Handbook of Crystal Growth* (Ref. [2]), Vol. 1b, p. 859.
[9] Y. Marietti, J.-M. Debierre, T. M. Bock, and K. Kassner, Phys. Rev. E **63**, 066301 (2001).
[10] Y. Marietti, J.-M. Debierre, T. M. Bock, and K. Kassner, Phys. Rev. E **63**, 066302 (2001).
[11] G. Müller and A. Ostrogorsky, in *Handbook of Crystal Growth* (Ref. [2]), Vol. 2b, p. 709.
[12] C. L. Marec, R. Guérin, and P. Haldenwang, Phys. Fluids **9**, 3149 (1997).
[13] H. Kopetsch, J. Cryst. Growth **102**, 505 (1990).
[14] F. Dupret and N. van den Bogaert, in *Handbook of Crystal Growth* (Ref. [2]), Vol. 2b, p. 875.
[15] A. Karma and W.-J. Rappel, Phys. Rev. Lett. **77**, 4050 (1996).
[16] R. Tönhardt and G. Amberg, J. Cryst. Growth **194**, 406 (1998).
[17] C. Beckermann *et al.*, J. Comput. Phys. **154**, 468 (1999).
[18] X. Tong, C. Beckermann, A. Karma, and Q. Li, Phys. Rev. E **63**, 061601 (2001).
[19] W. Miller, S. Succi, and D. Mansutti, Phys. Rev. Lett. **86**, 3578 (2001).
[20] W. Miller and S. Succi, J. Stat. Phys. **107**, 173 (2002).
[21] W. Miller, Int. J. Mod. Phys. B **17**, 227 (2003).
[22] D. Medvedev and K. Kassner, J. Cryst. Growth **275**, e1495 (2005).

[23] D. Medvedev and K. Kassner, Phys. Rev. E **72**, 056703 (2005).
[24] B. Caroli, C. Caroli, B. Roulet, and J. S. Langer, Phys. Rev. A **33**, 442 (1986).
[25] M. Ben Amar and Y. Pomeau, Europhys. Lett. **2**, 307 (1986).
[26] D. I. Meiron, Phys. Rev. A **33**, 2704 (1986).
[27] D. A. Kessler and H. Levine, Phys. Rev. B **33**, 7867 (1986).
[28] A. Barbieri, D. Hong, and J. S. Langer, Phys. Rev. A **35**, 1802 (1987).
[29] S. Tanveer, Phys. Rev. A **40**, 4756 (1989).
[30] M. Ben-Amar and E. Brener, Phys. Rev. Lett. **71**, 589 (1993).
[31] E. Brener, Phys. Rev. Lett. **71**, 3653 (1993).
[32] M. E. Glicksman and N. B. Singh, J. Cryst. Growth **98**, 277 (1989).
[33] Y. Saito, G. Goldbeck-Wood, and H. Müller-Krumbhaar, Phys. Rev. A **38**, 2148 (1988).
[34] T. Ihle and H. Müller-Krumbhaar, Phys. Rev. E **49**, 2972 (1994).
[35] A. Karma and W.-J. Rappel, Phys. Rev. E **57**, 4323 (1998).
[36] P. Pelcé, Europhys. Lett. **75**, 220 (2006).
[37] G. P. Ivantsov, Dokl. Akad. Nauk SSSR **58**, 567 (1947).
[38] M. Ben-Amar and E. Brener, Phys. Rev. Lett. **75**, 561 (1995).
[39] E. Brener, H. Müller-Krumbhaar, and D. Temkin, Phys. Rev. E **54**, 2714 (1996).
[40] P. Bouissou and P. Pelcé, Phys. Rev. A **40**, 6673 (1989).
[41] P. Bouissou, B. Perrin, and P. Tabeling, Phys. Rev. A **40**, 509 (1989).
[42] Y.-W. Lee, R. Ananth, and W. N. Gill, J. Cryst. Growth **132**, 226 (1993).
[43] S. Tanveer, J. Fluid Mech. **409**, 273 (2000).
[44] A. Karma and W.-J. Rappel, Phys. Rev. E **53**, R3017 (1996).
[45] R. Almgren, SIAM J. Appl. Math. **59**, 2086 (1999).
[46] S. Chen and G. Doolen, Annu. Rev. Fluid Mech. **30**, 329 (1998).
[47] Y. Qian, D. d'Humières, and P. Lallemand, Europhys. Lett. **17**, 479 (1992).
[48] A. Kupershtokh, in *Proceedings of the Fifth International EHD Workshop*, Poitiers, France, 2004, pp. 241–246.
[49] R. Kobayashi, Exp. Math. **3**, 60 (1994).
[50] X. Tong, C. Beckermann, and A. Karma, Phys. Rev. E **61**, R49 (2000).
[51] E. Brener and V. Mel'nikov, Adv. Phys. **40**, 53 (1991).
[52] A. Barbieri and J. S. Langer, Phys. Rev. A **39**, 5314 (1989).
[53] R. Kupferman, D. Kessler, and E. Ben-Jacob, Physica A **213**, 451 (1995).
[54] S. Tokunaga and H. Sakaguchi, Phys. Rev. E **70**, 011607 (2004).
[55] P. Saffman and G. Taylor, Proc. R. Soc. London, Ser. A **245**, 312 (1958).
[56] R. Combescot *et al.*, Phys. Rev. Lett. **56**, 2036 (1986).
[57] S. Akamatsu, G. Faivre, and T. Ihle, Phys. Rev. E **51**, 4751 (1995).
[58] I. Stalder and J. H. Bilgram, Europhys. Lett. **56**, 829 (2001).
[59] H. M. Singer and J. H. Bilgram, Phys. Rev. E **70**, 031601 (2004).